crystals

MDPI

Article

Synthesis and Characterization of New Organoammonium, Thiazolium, and Pyridinium Triiodide Salts: Crystal Structures, Polymorphism, and Thermal Stability

Madhushi Bandara [1], Khadijatul Kobra [1], Spencer R. Watts [1], Logan Grady [1], Connor Hudson [1], Claudina Veas [2], Timothy W. Hanks [2], Rakesh Sachdeva [1], Jorge Barroso [1], Colin D. McMillen [1,*] and William T. Pennington [1,*]

[1] Department of Chemistry, Clemson University, Clemson, SC 29634, USA; rakeshs@clemson.edu (R.S.); jabarro@clemson.edu (J.B.)
[2] Department of Chemistry, Furman University, Greenville, SC 29613, USA; nina.veas@furman.edu (C.V.); tim.hanks@furman.edu (T.W.H.)
* Correspondence: cmcmill@clemson.edu (C.D.M.); billp@clemson.edu (W.T.P.)

Abstract: Triiodide salts are of interest for a variety of applications, including but not limited to electrochemical and photochemical devices, as antimicrobials and disinfectants, in supramolecular chemistry and crystal engineering, and in ionic liquids and deep eutectic solvents. Our work has focused on the design of salt–solvate cocrystals and deep eutectic solvents in which the triiodide anion interacts as a halogen bond acceptor with organoiodine molecules. To understand structure–property relationships in these hybrid materials, it is essential to have benchmark structural and physical data for the parent triiodide salt component. Herein, we report the structure and thermal properties of eight new triiodide salts, three of which exhibit polymorphism: tetrapentylammonium triiodide (**1a** and **1b**), tetrahexylammonium triiodide (**2**), trimethylphenylammonium triiodide (**3**), trimethylbenzylammonium triiodide (**4**), triethylbenzylammonium triiodide (**5**), tri-*n*-butylbenzylammonium triiodide (**6**), 3-methylbenzothizolium triiodide (**7a** and **7b**), and 2-chloro-1-methylpyridinium triiodide (**8a** and **8b**). The structural features of the triiodide anion, Raman spectroscopic analysis, and melting and thermal decomposition behavior of the salts, as well as a computational analysis of the polymorphs, are discussed. The polymorphic pairs here are distinguished by symmetric versus asymmetric triiodide anions, as well as different packing patterns. Computational analyses revealed more subtle differences in their isosurface plots. Importantly, this study provides reference data for these new triiodide salts for comparison to hybrid cocrystals and deep eutectic solvents formed from their combination with various organoiodines.

Keywords: polymorphism; halogen bonding; crystallography; crystal structure; polyiodide salts; mechanochemistry; deep eutectic solvents

Citation: Bandara, M.; Kobra, K.; Watts, S.R.; Grady, L.; Hudson, C.; Veas, C.; Hanks, T.W.; Sachdeva, R.; Barroso, J.; McMillen, C.D.; et al. Synthesis and Characterization of New Organoammonium, Thiazolium, and Pyridinium Triiodide Salts: Crystal Structures, Polymorphism, and Thermal Stability. *Crystals* **2024**, *14*, 1020. https://doi.org/10.3390/cryst14121020

Academic Editor: Tom Leyssens

Received: 1 November 2024
Revised: 12 November 2024
Accepted: 15 November 2024
Published: 25 November 2024

1. Introduction

The triiodide anion represents the simplest and most common polyiodide anion in the structural literature [1–5]. Indeed, over 200 years ago, some of the first experimenters with iodine [6,7] documented the characteristic red color of what would ultimately be understood as the triiodide species [8,9]. The reaction of iodide salts with diiodine is now a well-known pathway toward the synthesis of triiodide salts [1]. Triiodides are now proving to be of interest in a variety of fields, including antimicrobials and disinfectants [10,11], electrochemistry and electrochemical devices [12–16], photochemistry/photophysics [17,18], reagents and catalysts in chemical synthesis [19,20], supramolecular chemistry and crystal engineering [21–26], and ionic liquids/deep eutectic solvents [27–30].

We have largely been interested in exploring how triiodides behave in these latter applications, where halogen bonding interactions between organoiodine molecules and triiodide anions can direct the formation of cocrystals or deep eutectic solvents. In these

applications, it is essential to have benchmark data related to the structure and properties of the parent triiodide salts to fully understand any influences of the halogen bonding in any cocrystals or deep eutectic solvents involving those triiodides. For example, in triiodide-organoiodine cocrystalline systems, the I-I bond lengths of the triiodide may be affected by halogen bonding interactions at one or both ends of the linear triiodide [23,24]. In deep eutectic solvent systems, knowledge of the melting points and melting enthalpies of the mixture components is essential to calculating the ideal eutectic profile for comparison with experimental data [31,32]. We recently found tetrapentylammonium triiodide (NPe_4I_3) and tetrahexylammonium triiodide ($NHex_4I_3$) form deep eutectic solvents with some organoiodines such as 1,2-diiodotetrafluorobenzene and 1,3-diiodotetrafluorobenzene [27]. Fundamental structural and thermal characterization of new triiodide salts such as these is thus needed.

Despite the ubiquitous nature of triiodide salts, their structural chemistry is far from exhausted (Figure 1). Crystal structures of the tetraalkylammonium triiodide salts, $N(alkyl)_4I_3$, are only reported for alkyl = methyl [33,34], ethyl [35], propyl [36], and butyl [37] substituents. To our knowledge, no structures of trialkylbenzylammonium triiodide salts have been reported. Likewise, the structures of trimethylphenylammonium triiodide, 3-methylbenzothiazolium triiodide, and 2-chloro-1-methylpyridinium triiodide have not been reported. Interestingly, some tendency toward polymorphism is observed among those triiodide salts reported in the structural literature. For example, tetramethylammonium triiodide is reported to have multiple polymorphic phase transitions with two structure types (*Pnnm* and $P2_1/c$) crystallographically characterized [34]. Tetraethylammonium triiodide displays polymorphism over two orthorhombic space groups, *Cmca* and *Pnma* [35]. Methyltriphenylphosphonium triiodide has been reported in an extensive set of five polymorphs, including two different polymorphs in *Pbca*, two different polymorphs in $P2_1/c$, and one polymorph in *P*-1 [38–40].

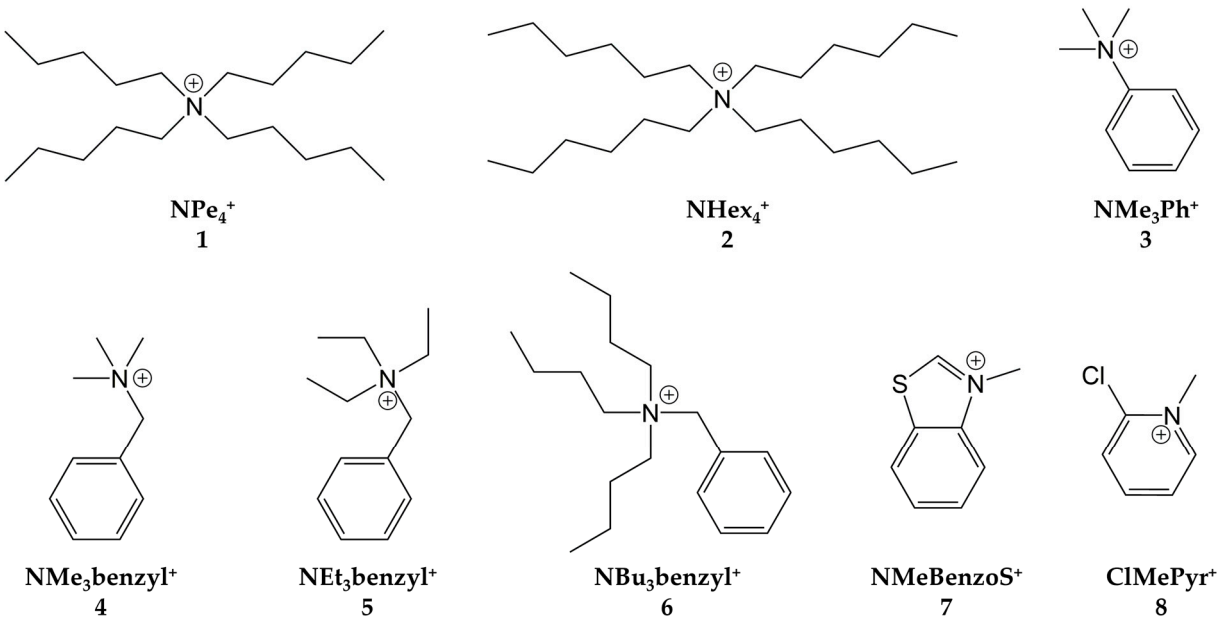

Figure 1. Organoammonium, thiazolium, and pyridinium cations prepared as triiodide salts in the present study, shown with shorthand notations and numbers used in this study.

The present study crystallographically characterizes eight new triiodide salts, three of which exhibit polymorphism (tetrapentylammonium triiodide (NPe_4I_3), 3-methylbenzothiazolium triiodide ($NMeBenzoSI_3$), and 2-chloro-1-methylpyridinium triiodide ($ClMePyrI_3$)). A computational analysis of the polymorphs is provided. The structural features of the triiodide anions, as well as the melting points of the salts, provide useful benchmarks for future studies in crystal engineering and deep eutectic solvents.

2. Materials and Methods

2.1. General Methods

Thermal Analysis: Simultaneous differential scanning calorimetry and thermal gravimetric analysis (DSC/TGA) measurements were made for each triiodide to determine the melting temperature and the decomposition profile. Data were collected using a TA Instruments (New Castle, DE, USA) SDT Q600 instrument and analyzed using TA Instruments Universal Analysis software (version 4.5A). Samples were heated from room temperature to 600 °C in nitrogen (100 mL min^{-1}) at a rate of 10 °C min^{-1}.

Raman Spectroscopy: Raman spectra were collected using a Horiba Scientific (Kyoto, Japan) XploRA PLUS Raman microscope with a Horiba TE Cooled detector operating at −60 °C. All data were collected using a 785 nm laser, a 1200 gr/mm grating, and a focal length of 200 mm. The 100 mW output power was reduced using a neutral density filter to 25–50% (depending on the sample) to avoid oversaturating the detector and to minimize sample heating. A 10× Olympus objective with a 10.6 mm working distance and an aperture of 0.25 was used for all samples. Data were collected using 10 sequential 10 s acquisitions.

Powder X-ray Diffraction: Powder X-ray diffraction data were collected using a Rigaku (Tokyo, Japan) Smartlab diffractometer with Cu Kα radiation (λ = 1.5408 Å) and a Hypix3000 detector. Data were collected in 0.02° steps from 5 to 45° in 2-theta at a rate of two degrees per minute.

2.2. Solution Synthesis and Crystal Growth

All solvents and reagents were used as received. Crystals for single-crystal X-ray diffraction measurements were obtained as follows.

Tetrapentylammonium triiodide (NPe_4I_3, **1a** and **1b**): Orthorhombic NPe_4I_3, **1a**, was synthesized using tetrapentylammonium iodide (NPe_4I, 0.034 g, 0.080 mmol) and I_2 (0.020 g, 0.079 mmol). The reagents were dissolved, with stirring, in 10 mL of methanol, and the solution was allowed to evaporate under ambient conditions. Red needle-like crystals of **1a** formed after about five days. Monoclinic NPe_4I_3, **1b**, was synthesized using NPe_4I (0.052 g, 0.12 mmol) and I_2 (0.031 g, 0.12 mmol) in the presence of thiourea (0.010 g, 0.13 mmol). The reagents were dissolved, with stirring, in a solution comprising 3 mL ethanol, 3 mL dichloromethane, and 3 mL acetonitrile. The solution was allowed to evaporate under ambient conditions. Red plate-like crystals of **1b** formed after about five days. The reaction product also contained colorless needle-like crystals of thiourea and pale yellow block-like crystals of sulfur.

Tetrahexylammonium triiodide ($NHex_4I_3$, **2**): $NHex_4I_3$, **2**, was synthesized using a two-step process of mechanochemical synthesis followed by recrystallization from solution. Tetrahexylammonium iodide ($NHex_4I$, 0.38 g, 0.79 mmol) and I_2 (0.20 g, 0.79 mmol) were hand-ground for three minutes using a mortar and pestle to produce a homogeneous red powder. A portion (0.08 g) of this powder (later found to be $NHex_4I_3$ by comparison of its powder diffraction pattern to that calculated from the single-crystal structure of $NHex_4I_3$; Supplementary Materials, Figure S1) was dissolved in 10 mL of methanol with stirring and gentle heating. The solution was allowed to evaporate under ambient conditions. Red plate-like crystals of **2** formed after about five days.

Trimethylphenylammonium triiodide (NMe_3PhI_3, **3**): NMe_3PhI_3, **3**, was synthesized using trimethylphenylammonium iodide (NMe_3PhI, 0.061 g, 0.23 mmol) and I_2 (0.059 g, 0.23 mmol). The reagents were dissolved, with stirring, in a solution comprising 3 mL ethanol, 3 mL dichloromethane, and 3 mL acetonitrile. The solution was allowed to evaporate under ambient conditions. Red plate-like crystals of **3** formed after about three days.

Trimethylbenzylammonium triiodide ($NMe_3BenzylI_3$, **4**): $NMe_3BenzylI_3$, **4**, was synthesized using trimethylbenzylammonium iodide ($NMe_3BenzylI$, 0.055 g, 0.20 mmol) and I_2 (0.050 g, 0.20 mmol). The reagents were dissolved, with stirring, in a solution comprising 3 mL ethanol, 3 mL dichloromethane, and 3 mL acetonitrile. The solution was allowed to evaporate under ambient conditions. Red plate-like crystals of **4** formed after about five days.

Triethylbenzylammonium triiodide ($NEt_3BenzylI_3$, **5**): $NEt_3BenzylI_3$, **5**, was synthesized using triethylbenzylammonium iodide ($NEt_3BenzylI$, 0.052 g, 0.16 mmol) and I_2 (0.041 g, 0.16 mmol). The reagents were dissolved, with stirring, in 15 mL of methanol, and the solution was allowed to evaporate under ambient conditions. Red block-like crystals of **5** formed after about two weeks, with an additional red, thick liquid presumed to be a polyiodide product with a melting point below room temperature.

Tributylbenzylammonium triiodide ($NBu_3BenzylI_3$, **6**): $NBu_3BenzylI_3$, **6**, was synthesized using a two-step process of mechanochemical synthesis followed by recrystallization from solution. Tributylbenzylammonium iodide ($NBu_3BenzylI$, 0.32 g, 0.79 mmol) and I_2 (0.20 g, 0.79 mmol) were hand-ground for three minutes using a mortar and pestle to produce a homogeneous red powder. A portion (0.06 g) of this powder (later found to be primarily $NBu_3BenzylI_3$ by comparison of its powder diffraction pattern to that calculated from the single-crystal structure of $NBu_3BenzylI_3$; Supplementary Materials, Figure S2) was dissolved in 10 mL of methanol, with stirring and gentle heating. The solution was allowed to evaporate under ambient conditions. Red plate-like crystals of **6** formed after about five days.

3-methylbenzothiazolium triiodide ($NMeBenzoSI_3$, **7a** and **7b**): Monoclinic $NMeBenzoSI_3$, **7a**, was synthesized using 3-methylbenzothiazolium iodide (NMeBenzoSI, 0.022 g, 0.079 mmol) and I_2 (0.020 g, 0.079 mmol). The reagents were dissolved, with stirring, in 10 mL of methanol, and the solution was allowed to evaporate under ambient conditions. Red needle-like crystals of **7a** formed after about five days. Triclinic $NMeBenzoSI_3$, **7b**, was synthesized from NMeBenzoSI (0.031 g, 0.11 mmol) and excess I_2 (0.085 g, 0.33 mmol). The reagents were dissolved, with stirring, in a solution comprising 3 mL ethanol, 3 mL dichloromethane, and 3 mL acetonitrile. The solution was allowed to evaporate under ambient conditions. Red block-like crystals of **7b** formed after about seven days. The reaction product also contained a thick red liquid, which is presumed to be a polyiodide product with a melting point below room temperature.

2-chloro-1-methylpyridinium triiodide ($ClMePyrI_3$, **8a** and **8b**): Monoclinic ($P2_1/n$) $ClMePyrI_3$, **8a**, was synthesized using 2-chloro-1-methylpyridinium iodide (ClMePyrI, 0.036 g, 0.14 mmol) and I_2 (0.035 g, 0.14 mmol) in the presence of 2,5-diiodothiophene (0.095 g, 0.28 mmol). The reagents were dissolved, with stirring, in a solution comprising 5 mL ethanol, 5 mL dichloromethane, and 5 mL acetonitrile. The solution was allowed to evaporate under ambient conditions. Red plate-like crystals of **8a** formed after about ten days, along with colorless tabular crystals of 2,5-diiodothiophene. Monoclinic ($P2/c$) $ClMePyrI_3$, **8b**, was synthesized using ClMePyrI (0.020 g, 0.079 mmol) and I_2 (0.020 g, 0.079 mmol). The reagents were dissolved, with stirring, in 15 mL of methanol. The solution was allowed to evaporate under ambient conditions. Red block-like crystals of **8b** formed after about ten days near the top of the reaction vial. The reaction product also contained red plate-like crystals near the bottom of the reaction vial, which were found to be a higher polyiodide species that will be discussed in a separate report.

2.3. Mechanochemical Synthesis in Polymorphic Systems

Mechanochemical synthesis was also explored for systems exhibiting polymorphic behavior to identify if one of the polymorphic phases predominated from that approach. For NPe_4I_3, **1a** and **1b**, a 1:1 molar ratio of NPe_4I (0.60 g, 1.4 mmol) and I_2 (0.36 g, 1.4 mmol) was hand-ground for three minutes using a mortar and pestle, producing a red polycrystalline powder. For $NMeBenzoSI_3$, **7a** and **7b**, a 1:1 molar ratio of NMeBenzoSI (0.50 g, 1.8 mmol) and I_2 (0.46 g, 1.8 mmol) was hand-ground for three minutes using a mortar and pestle, producing a red polycrystalline powder. For $ClMePyrI_3$, **8a** and **8b**, a 1:1 molar ratio of ClMePyrI (0.20 g, 0.79 mmol) and I_2 (0.20 g, 0.79 mmol) was hand-ground for three minutes using a mortar and pestle, producing a red polycrystalline powder. Powder X-ray diffraction patterns of these mechanochemical syntheses are provided in the Supplementary Materials, Figures S3–S5.

2.4. Single-Crystal X-Ray Diffraction

Single-crystal X-ray diffraction data were collected in a cold nitrogen stream using Bruker (Madison, WI, USA) D8 Venture and Bruker D8 Quest diffractometers. The data were collected using phi and omega scans (0.50° oscillations) with Mo Kα radiation (λ = 0.71073 Å) and a Photon 100 or Photon 3 detector. Data were processed (SAINT) and corrected for absorption using multi-scan techniques (SADABS), both within the Apex3 suite [41]. The structures were solved by intrinsic phasing and subsequently refined by full-matrix least squares on F^2 using the SHELXTL software package [42,43]. All non-hydrogen atoms were refined anisotropically. Hydrogen atoms attached to carbon atoms were refined in calculated positions using the appropriate riding models. The structure of **4** was refined as a two-component pseudo-merohedral twin with a batch scale factor refined to 0.39. The structure of **1a** was refined to include symmetry-imposed disorder of the pentyl arms of the tetrapentylammonium cation. All four pentyl substituents were refined at general positions with half occupancy. The structure of **8b** exhibited disorder of the 2-chloro-1-methylpyridinium cation, where two overlapping orientations were apparent. These were refined in two parts, with the occupancies freely refined in a 0.83:0.17 ratio. Several similarity restraints were utilized in these two disordered structures to maintain chemically reasonable anisotropic displacement parameters of disordered atoms. Complete refinement details are summarized in Tables 1 and 2. CCDC 2,376,730–2,376,740 contain the supplementary crystallographic data for this paper and can be obtained from the Cambridge Crystallographic Data Centre.

Table 1. Crystallographic data for triiodides **1**–**5**.

	1a NPe_4I_3	**1b** NPe_4I_3	**2** $NHex_4I_3$	**3** NMe_3PhI_3	**4** $NMe_3BenzylI_3$	**5** $NEt_3BenzylI_3$
Formula	$C_{20}H_{44}I_3N$	$C_{20}H_{44}I_3N$	$C_{24}H_{52}I_3N$	$C_9H_{14}I_3N$	$C_{10}H_{16}I_3N$	$C_{13}H_{22}I_3N$
F. W. (g/mol)	679.26	679.26	735.36	516.91	530.94	573.01
Temperature (K)	100(2)	140(2)	150(2)	100(2)	100(2)	130(2)
Crystal system	Orthorhombic	Monoclinic	Monoclinic	Orthorhombic	Monoclinic	Monoclinic
Space group	*Pbcm*	*C*2/*c*	*C*2/*c*	*Pnma*	$P2_1/c$	$P2_1/c$
a (Å)	11.4939(4)	21.5453(15)	14.3336(6)	7.0075(5)	9.4304(11)	9.3857(8)
b (Å)	21.1725(8)	10.2589(7)	16.6320(7)	8.1709(6)	17.402(2)	16.6742(14)
c (Å)	11.3399(4)	13.6585(9)	13.0010(5)	24.4498(17)	18.279(2)	11.9472(10)
α (°)	90	90	90	90	90	90
β (°)	90	116.991(2)	104.1564(14)	90	90.190(4)	112.896(3)
γ (°)	90	90	90	90	90	90
Volume (Å^3)	2759.62(17)	2690.1(3)	3005.3(2)	1399.94(17)	2999.7(6)	1722.4(3)
Z	4	4	4	4	8	4
D (calcd) (g/cm^3)	1.635	1.677	1.625	2.453	2.351	2.210
μ (mm^{-1})	3.401	3.489	3.130	6.664	6.223	5.428
F (000)	1320	1320	1448	936	1936	1064
Cryst. size (mm)	0.28, 0.06, 0.03	0.10, 0.10, 0.03	0.16, 0.12, 0.05	0.20, 0.10, 0.02	0.22, 0.15, 0.02	0.28, 0.12, 0.06
Detector	Photon 100	Photon 100	Photon 100	Photon 100	Photon 100	Photon 3
θ range (°)	2.62 to 25.50	3.04 to 26.42	3.80 to 26.44	2.63 to 28.31	2.16 to 26.89	3.07 to 29.12
Reflns. collected	21653	17105	32063	10998	69050	45695
Indep. reflns.	2695	2758	3089	1859	6435	4617
R (int)	0.0434	0.0603	0.0393	0.0517	0.0809	0.0590
No. of parameters	209	111	128	72	260	157
No. of restraints	24	0	0	0	0	0
R indices (I > 2σ (I))	R1 = 0.0445 wR2 = 0.1143	R1 = 0.0339 wR2 = 0.0446	R1 = 0.0368 wR2 = 0.0686	R1 = 0.0266 wR2 = 0.0523	R1 = 0.0354 wR2 = 0.0774	R1 = 0.0269 wR2 = 0.0571
R indices (All data)	R1 = 0.0572 wR2 = 0.1195	R1 = 0.0557 wR2 = 0.0489	R1 = 0.0570 wR2 = 0.0767	R1 = 0.0383 wR2 = 0.0555	R1 = 0.0467 wR2 = 0.0828	R1 = 0.0321 wR2 = 0.0619
S	1.278	1.044	1.053	1.053	1.051	1.052
Largest diff. peak/hole (eÅ^{-3})	0.660, −0.815	0.730, −0.635	1.248, −1.862	0.919, −0.725	0.786, −1.414	0.983, −0.862
CCDC dep. no.	2,376,730	2,376,731	2,376,732	2,376,733	2,376,734	2,376,735

Table 2. Crystallographic data for triiodides **6**–**8**.

	6 **$NBu_3BenzylI_3$**	**7a** **$NMeBenzoSI_3$**	**7b** **$NMeBenzoSI_3$**	**8a** **$ClMePyrI_3$**	**8b** **$ClMePyrI_3$**
Formula	$C_{19}H_{34}I_3N$	$C_8H_8I_3NS$	$C_8H_8I_3NS$	$C_6H_7ClI_3N$	$C_6H_7ClI_3N$
F. W. (g/mol)	657.17	530.91	530.91	509.28	509.28
Temperature (K)	100(2)	100(2)	140(2)	100(2)	100(2)
Crystal system	Monoclinic	Monoclinic	Triclinic	Monoclinic	Monoclinic
Space group	$P2_1/c$	$P2_1/n$	P-1	$P2_1/n$	$P2/c$
a (Å)	14.3571(7)	7.8959(3)	7.2564(4)	7.4306(6)	12.3893(5)
b (Å)	8.5155(4)	10.8757(5)	9.7552(5)	11.7159(9)	6.3108(3)
c (Å)	19.6725(9)	15.0940(6)	10.8679(6)	14.0973(11)	16.1478(7)
α (°)	90	90	68.1036(19)	90	90
β (°)	90.4745(18)	95.2290(13)	86.239(2)	101.167(2)	107.4464(14)
γ (°)	90	90	70.265(2)	90	90
Volume (Å^3)	2405.0(2)	1290.78(9)	670.28(6)	1204.02(16)	1204.46(9)
Z	4	4	2	4	4
D (calcd) (g/cm^3)	1.815	2.732	2.631	2.809	2.808
μ (mm^{-1})	3.900	7.387	7.113	7.960	7.957
F (000)	1256	952	476	904	904
Cryst. size (mm)	0.24, 0.05, 0.03	0.17, 0.03, 0.03	0.09, 0.04, 0.04	0.24, 0.19, 0.04	0.18, 0.09, 0.04
Detector	Photon 100	Photon 100	Photon 100	Photon 100	Photon 3
θ range (°)	2.50 to 27.91	3.38 to 26.42	2.39 to 28.32	2.28 to 30.56	3.66 to 27.16
Reflns. collected	48,095	22,116	25,766	70,939	30,317
Indep. reflns.	5737	2638	3324	3676	2656
R (int)	0.0481	0.0522	0.0446	0.0331	0.0541
No. of parameters	212	119	123	100	121
No. of restraints	0	0	0	0	40
R indices (I > 2σ(I))	R1 = 0.0235 wR2 = 0.0363	R1 = 0.0276 wR2 = 0.0402	R1 = 0.0273 wR2 = 0.0521	R1 = 0.0396 wR2 = 0.1054	R1 = 0.0328 wR2 = 0.0725
R indices (All data)	R1 = 0.0361 wR2 = 0.0389	R1 = 0.0440 wR2 = 0.0438	R1 = 0.0399 wR2 = 0.0556	R1 = 0.0405 wR2 = 0.1058	R1 = 0.0376 wR2 = 0.0755
S	1.015	1.044	1.038	1.298	1.039
Largest diff. peak/hole (eÅ^{-3})	0.443, −0.552	0.729, −0.718	2.064, −0.873	2.473, −2.068	1.313, −0.960
CCDC dep. no.	2,376,736	2,376,737	2,376,738	2,376,739	2,376,740

2.5. Computational Methodology

The DFT calculations were carried out through the PBEsol exchange–correlation functional [44], as implemented in the Quantum Espresso version 5.4 software [45,46]. The corresponding SSSP PBESol Efficiency pseudopotentials were taken from the Computational Materials database [47]. The van der Waals forces were considered using Grimme's D3 approach [48]. The energy and charge density cutoffs were set at 60 and 480 Ry, respectively, within a 10^{-8} convergence threshold for the self-consistency cycle. Additionally, a Periodic Energy Decomposition Analysis (PEDA) [49] was performed at the all-electron SCAN-D3(BJ)/DZP level [50–53] to better understand the interaction between the fragments formed by the triiodides and the nitrogen derivatives. The PEDA breaks down the interaction energy, ΔE_{int}, into four physically meaningful terms, as follows:

$$\Delta E_{int} = \Delta E_{Pauli} + \Delta V_{elstat} + \Delta E_{orb} + \Delta E_{disp}$$

where ΔE_{Pauli} is the repulsive term associated with electrons with the same spin, ΔV_{elstat} is the quasi-classical Coulombic interaction, ΔE_{orb} results from stabilizing the crystal orbitals with respect to the corresponding fragments, and ΔE_{disp} accounts for the weak van der Waals forces. As weak interactions are essential in favoring one polymorph over another, the identification and visualization of non-covalent interactions (NCIs) between the triiodide fragments and ammonium derivatives within the crystal were estimated by evaluating the NCI indices based on the ratio between the gradient and reduced gradient of the electron

density [54]. The resulting isosurfaces were plotted using the IGMPLOT program [55,56], where the color code reveals whether the intermolecular regions have weak (green) or strong (blue) interactions or repulsive (red).

3. Results and Discussion

3.1. Synthesis and Crystal Structures

The structures of the triiodide salts are shown in Figure 2, with triiodide geometries summarized in Table 3. Solution synthesis approaches to NPe_4I_3 produced two polymorphs, **1a** and **1b**, crystallizing in *Pbcm* and *C*2/*c*, respectively. The polymorph structures are distinguishable by their packing structures and the asymmetric versus symmetric nature of their respective triiodide anions. In **1a**, all three iodine atoms of the triiodide anion sit on 4d Wyckoff sites, and the triiodide is asymmetric (Δ I-I = 0.0824 Å). The nitrogen atom of the NPe_4^+ cation likewise sits on a 4d Wyckoff site, and its substituent pentyl arms are disordered by symmetry, with these atoms half occupied at general positions. The anions and cations stack in alternating fashion along the *b*-axis, with triiodide anions spanning between neighboring columns of NPe_4^+ cations that are stacked along the *a*-axis (Figure 3). In **1b,** the triiodide anions are symmetric, having inversion symmetry. The packing structure indicates a layered arrangement of anion and cation layers alternating along the *c*-axis (Figure 3). Given the occurrence of both polymorphs from solution reactions differing in solvent identity (methanol for **1a** and a mixture of ethanol, dichloromethane, and acetonitrile for **1b**), we pursued a mechanochemical synthesis to see if one form was preferred from that approach. Powder diffraction data (Supplementary Materials, Figure S3) suggest that a majority of the product is the orthorhombic polymorph **1a**. However, weaker peaks in the experimental data corresponding to the monoclinic polymorph **1b** are also represented. A pure sample of **1a** was obtained from the crystals harvested from solution synthesis in methanol, enabling a reliable melting point measurement, as reported below.

Triiodide salts **2**–**6** did not exhibit polymorphic behavior in our hands, but their structures are briefly discussed here. The synthesis of **2** is worth particular comment since direct reactions of $NHex_4I + I_2$ in various solvents did not yield suitable crystals for analysis. An alternative approach was taken to react $NHex_4I + I_2$ mechanochemically, which produced a red powder, and then to recrystallize that powder. Recrystallization in methanol fortunately produced red single crystals, **2**. The structure of **2** features a symmetric triiodide anion with two-fold rotational symmetry and a symmetric $NHex_4^+$ cation, which also has two-fold rotational symmetry through its nitrogen atom. The long hexyl substituents of the cations form a framework containing channels (Supplementary Materials, Figure S6) along the *a*-axis in which the triiodide anions reside (though the linear axes of the triiodide anions are not oriented directly along the *a*-axis). The packing of anions and cations alternates along the *b*- and *c*-axes. A comparison of the calculated powder diffraction pattern from the single-crystal structure to the precursor red powder obtained by mechanochemistry suggests they are identical species, and the crystal growth successfully proceeded through simple recrystallization.

The triiodide salts **3**–**6** (packing diagrams in the Supplementary Materials, Figures S7–S10) are based on cationic species that contain three alkyl and one phenyl or benzyl substituent to form the organoammonium cation, potentially introducing C-H···π or π···π stacking contacts. All these salts displayed asymmetric triiodides with distortion ranging from Δ I-I = 0.0051 Å in **3** to 0.0746 Å in one of the two unique triiodides in **4**. The packing structure of **3** features alternating anions and cations along the *b*-axis and alternating pairs of anions and cations along the c-axis. In particular, the cation pairs display a C-H···π contact with H···centroid of 2.606 Å and C-H···centroid = 177.7° (Supplementary Materials, Figure S11). C-H···I contacts occur at only one end of the triiodide anion but serve to extend the long-range structure. The packing structure of **4** contains stacks of NMe_3benzyl$^+$ cations and triiodide anions along the *a*-axis, with alternating anion and cation stacks occurring along the *b*- and *c*-axes. The long-range structure of short contacts involves C-H···I interactions between cations and anions. The NEt_3benzylI_3 salt, **5**, packs with a

layered pattern of cation layers and anion layers alternating along the *b*-axis. Within the cation layers, the $NEt_3benzyl^+$ cations form dimers through C-H···π interactions involving hydrogen atoms of CH_2 carbon atoms oriented toward the edge of a neighboring benzene ring (Supplementary Materials, Figure S12). In **6**, cations and anions stack in alternating fashion along the *a*- and *b*-axes. Similar to **2**, the bulkier cations create a channel-like framework along the *c*-axis in which the triiodide anions reside. The intermolecular short contacts occurring in **6** are C-H···I interactions between the alternating anions and cations along the *b*-axis. Also similar to **2**, **6** required the two-step process of mechanochemistry followed by recrystallization from methanol in order to obtain suitable single crystals.

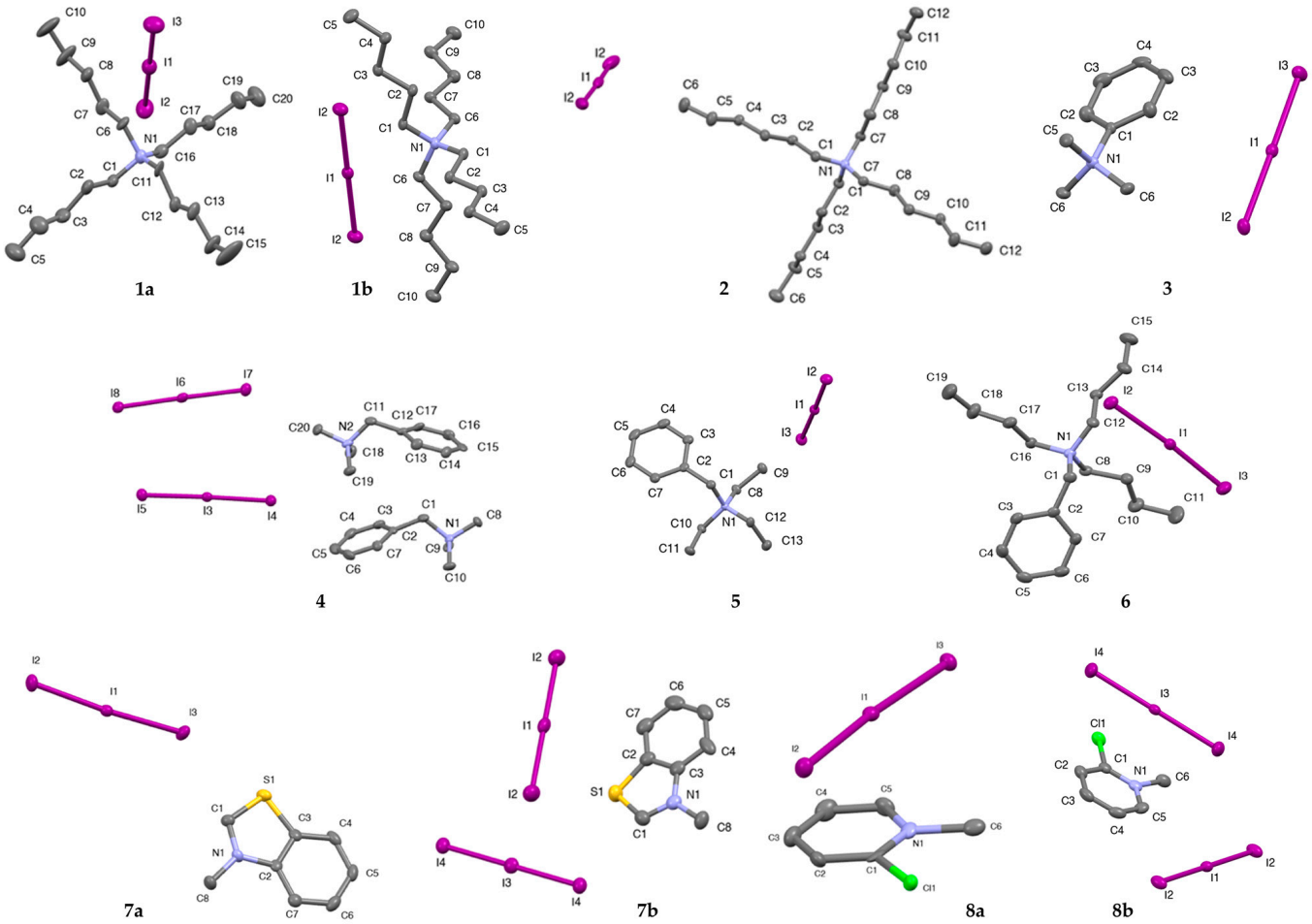

Figure 2. Crystal structures of triiodides **1**–**8**, shown as 50% probability ellipsoids. Hydrogen atoms are omitted for clarity. Note that extended asymmetric units are shown for triiodides **1b**, **2**, **7b**, and **8b** in order to show complete molecules. In these cases, the central atom of the triiodide anions sits on a special position, with the remaining two iodine atoms produced from only one unique iodine atom at a general position. In this way, there are two unique half-triiodides in the asymmetric unit of **7b** and **8b**, both expanded to their full triiodide geometry but shown with only one cation.

Table 3. Triiodide geometries in compounds **1**–**8**. Two I-I bond lengths are provided, I-I_a and I-I_b, occurring from the central iodine atom to the terminal iodine atoms of the triiodide anion. Δ I-I is the difference in these bond lengths as a means of quantifying triiodide asymmetry. If multiple triiodide anions occur in the asymmetric unit (as in **4**, **7b**, and **8b**), their geometries are provided in separate rows.

Compound	I-I_a (Å)	I-I_b (Å)	Δ I-I (Å)	I-I-I (°)
1a	2.8727(11)	2.9551(11)	0.0824	178.95(4)
1b	2.9232(3)	2.9232(3)	-	180
2	2.9384(5)	2.9384(5)	-	176.63(2)
3	2.9215(5)	2.9266(5)	0.0051	178.99(1)
4	2.8808(8)	2.9554(8)	0.0746	175.43(2)
	2.8907(8)	2.9306(8)	0.0399	178.74(3)
5	2.9097(3)	2.9410(3)	0.0313	178.69(1)
6	2.8984(3)	2.9461(3)	0.0477	175.62(1)
7a	2.8928(5)	2.9310(5)	0.0382	175.21(2)
7b	2.9197(3)	2.9197(3)	-	180
	2.9257(3)	2.9257(3)	-	180
8a	2.8425(7)	3.0378(7)	0.1953	176.25(2)
8b	2.9200(4)	2.9200(4)	-	180
	2.8961(4)	2.8961(4)	-	179.18(3)

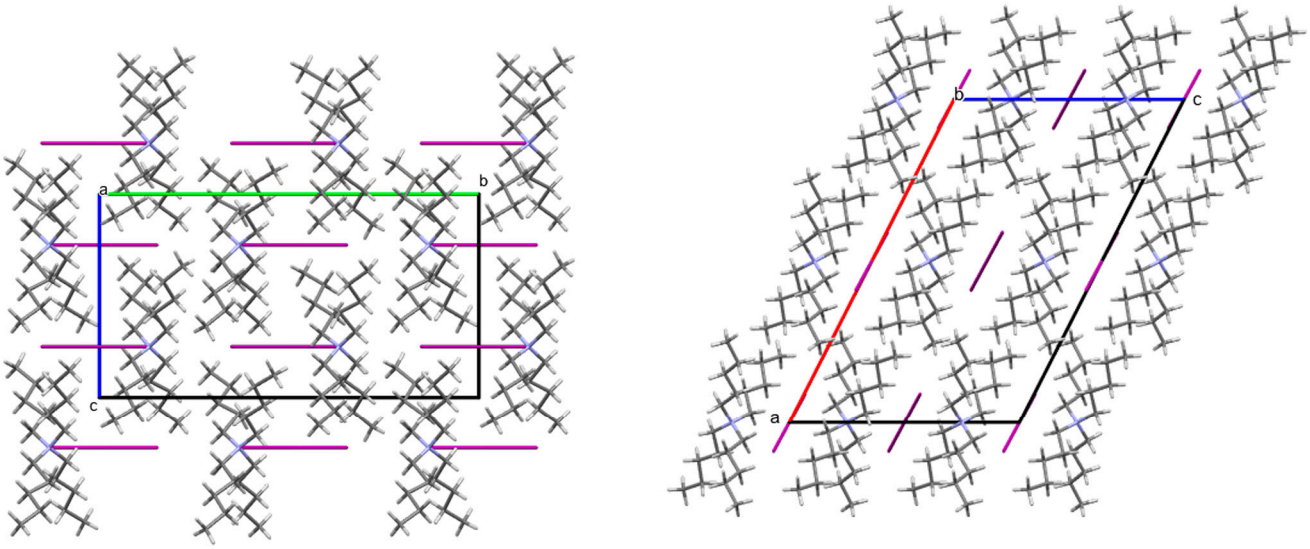

1a **1b**

Figure 3. Packing diagrams of NPe_4I_3 polymorphs **1a** and **1b**, viewed along the *a*-axis and *b*-axis, respectively. Unit cell axis designations are *a*-axis = red, *b*-axis = green, and *c*-axis = blue. Iodine atoms are shown in dark purple, nitrogen atoms in light purple, carbon atoms in gray, and hydrogen atoms in white.

The thiazolium system $NMeBenzoSI_3$ also resulted in two polymorphs (**7a** and **7b**, Figure 4), with **7a** crystallizing in $P2_1/n$ and **7b** crystallizing in $P\text{-}1$. The polymorphs again occurred from reactions differing in both the amount of I_2 used and the solvent identity (**7a** occurring from a 1:1 ratio of $NMeBenzoSI:I_2$ in methanol and **7b** occurring from a 1:3 ratio of $NMeBenzoSI:I_2$ in a mixture of ethanol, dichloromethane, and acetonitrile). The polymorphs are again distinguished by the asymmetric triiodide anion (Δ I-I = 0.0382 Å) in **7a** versus the symmetric triiodide in **7b**. The presence of sulfur on the cation makes this system additionally susceptible to differences in intermolecular contacts related to halogen or chalcogen bonding. In **7a**, anions and cations form alternating layers parallel to (−1 0 1). This results in the anions and cations alternating individually along all three

unit cell axes. Chains of I···S interactions occur along [−1 0 1], linking the layers of anions and cations. The I···S interactions occur toward the electropositive region capping the ends of the triiodide anions, with I···S distances of 3.6097(13) Å and 3.7634(12) Å and I-I···S angles of 140.77(2)° and 151.01(2)°, consistent with halogen bonding interactions. Here, the shorter I···S halogen bond is associated with the longer I-I bond of the triiodide. In **7b**, the presence of two unique symmetric triiodide anions (half of each molecule is unique, sitting on inversion centers) changes the nature of the layers that are formed. This appears to be driven by different intermolecular interactions in **7b**, where symmetric S···I interactions (S···I = 3.6899(12) Å) sandwich one triiodide anion between two cations, while the second triiodide anion maintains no short contacts within the sum of the van der Waals radii. The S···I interactions here are characteristic of a chalcogen bonding interaction, occurring from one of the electropositive caps on a C-S bond to the electronegative region on the side of the terminal iodine atoms of the triiodide (C-S···I = 156.74(14)° and S···I-I = 97.38(2)°). Mechanochemistry was again pursued to identify the preferred polymorph from that synthetic approach. Powder X-ray diffraction indicated a predominance of **7a** with a minor contribution of **7b** (Supplementary Materials, Figure S4).

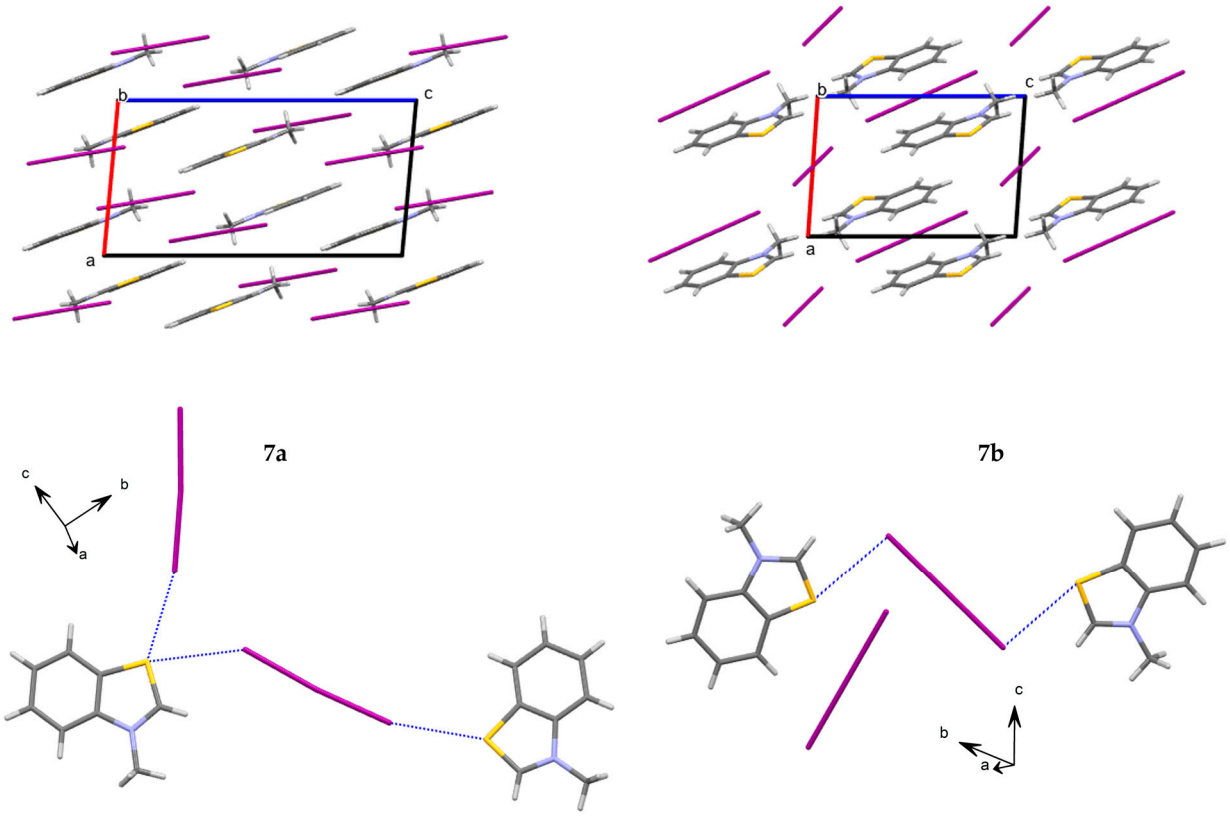

Figure 4. Packing diagrams (top) of NMeBenzoSI$_3$ polymorphs **7a** and **7b**, viewed along the *b*-axis, and I···S/S···I interactions (bottom, blue dashed lines) occurring in polymorphs **7a** and **7b**. Unit cell axis designations are *a*-axis = red, *b*-axis = green, and *c*-axis = blue. Iodine atoms are shown in dark purple, nitrogen atoms in light purple, sulfur atoms in yellow, carbon atoms in gray, and hydrogen atoms in white.

The pyridinium system, ClMePyrI$_3$ (**8a** and **8b**), exhibited polymorphism (Figure 5) across two monoclinic space groups, $P2_1/n$ for **8a** and $P2/c$ for **8b**. They again differ in the asymmetric (**8a**) versus symmetric (**8b**) nature of the triiodide anions and in the nature of the solvent from which they were synthesized (**8a** from a mixture of ethanol, dichloromethane, and acetonitrile, and **8b** from methanol). The triiodide anion in **8a** is the most asymmetric of the salts in the current study, with Δ I-I = 0.1953 Å. This may indicate

movement toward a halogen-bonded $I_2 \cdots I$ interaction, and while the I-I-I bond lengths are near the short and long ends of what are typically classified as triiodides, they still remain in range to be considered to be an I_3^- entity [2]. The cations and anions pack in alternating fashion along the *a*-axis and *c*-axis and in alternating but slightly offset fashion along the *b*-axis. The resulting intermolecular interactions show the formation of halogen-bonded triiodide chains (I···I = 3.9372(7) Å) involving the anions and cationic chains formed by C-H···Cl interactions. Both chains propagate along the *b*-axis. The offset nature of the cation and anion packing along the *b*-axis allows the chains to propagate in parallel, where the zigzag triiodide chains accommodate the methyl groups extending from the pyridinium chains. In **8b**, packing occurs in a layered fashion, with anion and cation layers stacked in alternating fashion along the *a*-axis. The two unique triiodide anions (again present as two unique half molecules in the asymmetric unit, one having inversion symmetry and the other having two-fold rotational symmetry) show different short contacts in the structure. One of the triiodide anions is oriented to be a Cl···I halogen bond acceptor sandwiched between two cations (Cl···I = 3.7142(15) Å and 3.8564(17) Å). The other triiodide anion is pinned in place by numerous C-H···I interactions. Mechanochemical synthesis of ClMePyrI + I_2 produced polymorph **7b**, with no detectable presence of **7a** based on powder X-ray diffraction (Supplementary Materials, Figure S5).

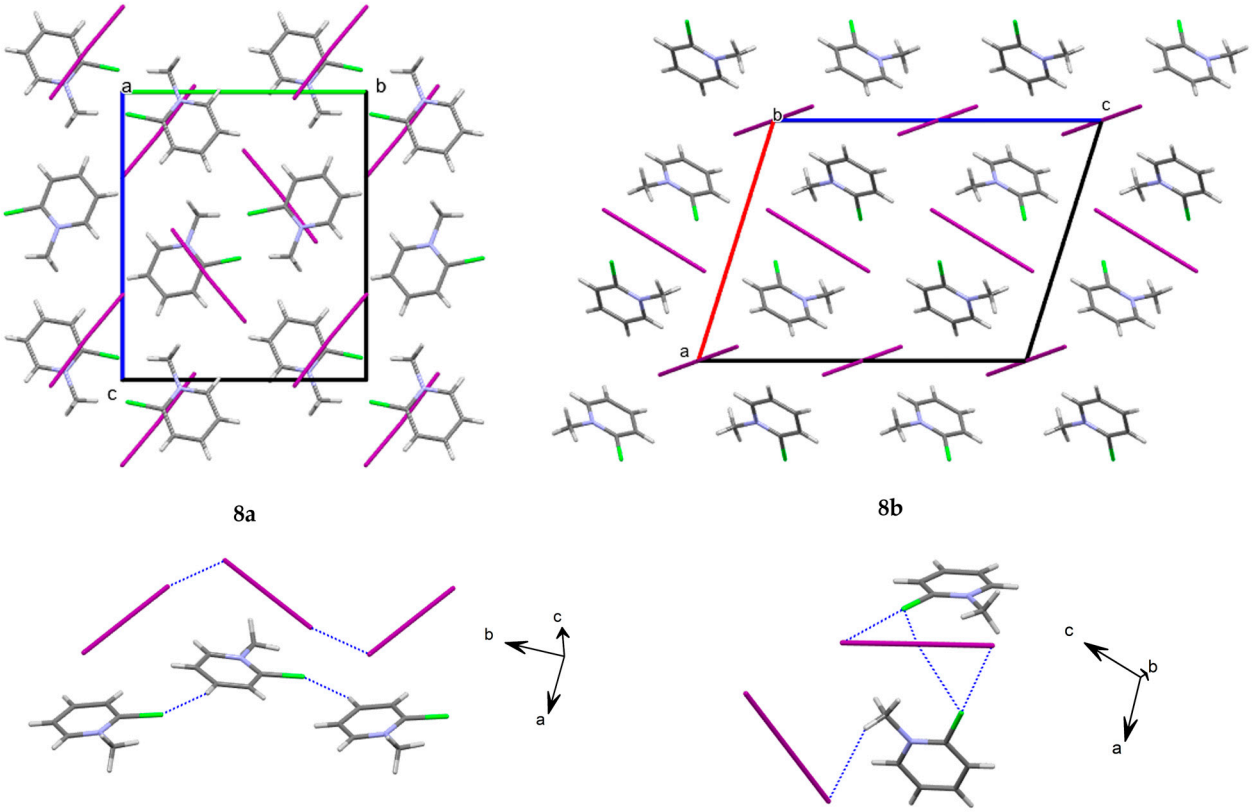

Figure 5. Packing diagrams (top) of $ClMePyrI_3$ polymorphs **8a** and **8b**, viewed along the *a*-axis and *b*-axis, respectively, and selected intermolecular interactions (bottom, blue dashed lines) occurring in polymorphs **8a** and **8b**. Unit cell axis designations are *a*-axis = red, *b*-axis = green, and *c*-axis = blue. Iodine atoms are shown in dark purple, nitrogen atoms in light purple, chlorine atoms in green, carbon atoms in gray, and hydrogen atoms in white. Only the major component of the cation disorder in **8b** is shown.

3.2. Computational Evaluation of Polymorphs

For additional exploration of the preference of one polymorph over the other, we performed DFT calculations (Table 4, Figure 6) with periodic boundary conditions. The

nature of the interaction between the iodine atoms and the ammonium units was characterized by a Periodic Energy Decomposition Analysis (PEDA). This analysis decomposes the interaction energy, ΔE_{int}, into specific physical terms, i.e., the Coulombic electrostatic interaction, ΔV_{elstat}, the orbital interaction, ΔE_{orb}, and weak van der Waals dispersion forces, ΔE_{disp}. The analysis also includes the repulsive counterpart associated with the Pauli exclusion, which includes the destabilizing steric fraction between the occupied orbitals of the fragments. For instance, the PEDA indicates that the interaction energy between the triiodide and tetrapentylammonium fragments in **1a** is −798.4 kcal/mol per unit cell, which is significantly lower than **1b**, −1194.0 kcal/mol. The main destabilizing factor in **1b** is apparently due to Pauli repulsion, almost doubling the value of **1a**. This remarkable difference might be explained by the cation disordering in **1a**. That is, the fully ordered arrangement of cations in **1b** favors higher interaction energy within fragments. Despite the noticeable difference in the strength of interaction between the fragments in the tetrapentylammonium triiodide polymorphs, the way they interact is similar. The interaction is predominantly orbital (88.0–91.3%) and with electrostatic and dispersion contributions of less than 10%. Weak interactions between fragments are represented as green isosurfaces in Figure 6. Noticeably, the contacts in **1a** are between iodine and hydrogen atoms, while in **1b**, more ordered contacts are found, as well as some I···CH_2 interactions.

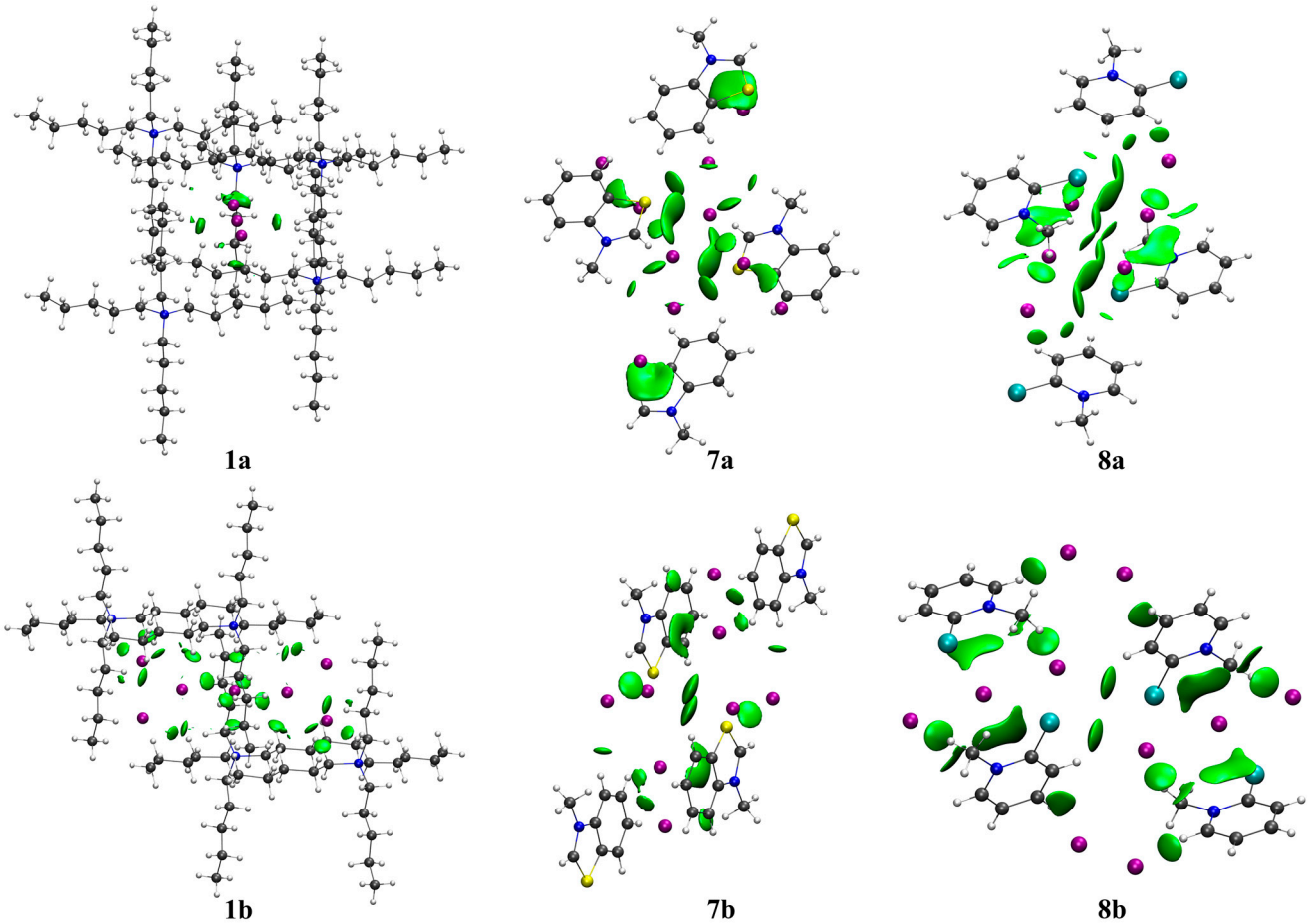

Figure 6. Non-covalent interactions (NCIs) plot of the triiodide polymorphs. Green isosurfaces represent weak van der Waals interactions. The corresponding isovalues are 0.3 a.u.

Table 4. PEDA considering the triiodide and ammonium fragments within polymorphs. The analysis is computed using an all-electron SCAN-D3(BJ)/DZP level. The values within parentheses show the percentage of the total attractive contributions.

	ΔE_{int}	ΔE_{Pauli}	Steric	ΔV_{elstat}	ΔE_{orb}	ΔE_{disp}
1a	−798.4	97.4	65.3	−32.1 (3.6)	−817.8 (91.3)	−46.0 (5.1)
1b	−1171.9	184.7	68.7	−116.0 (8.6)	−1194.0 (88.0)	−46.6 (3.4)
7a	−416.3	78.4	0.9	−77.5 (15.7)	−378.9 (76.6)	−38.3 (7.7)
7b	−422.8	66.6	6.6	−60.0 (12.3)	−393.8 (80.4)	−35.8 (7.3)
8a	−393.7	70.3	−3.7	−74.0 (17.1)	−355.3 (81.9)	−34.7 (7.4)
8b	−402.4	66.9	−3.7	−70.6 (12.2)	−364.5 (63.1)	−143.0 (24.7)

Regarding the thiazolium systems, the DFT calculations using PBEsol indicate that the lattice energy of **7a** is only 2.6 kcal/mol more stable than **7b**. However, the triiodide fragments interact with the 3-methylbenzothiazolium moieties slightly stronger in the former by about 6.5 kcal/mol according to the PEDA at an all-electron SCAN-D3(BJ)/DZP level. The most notable difference is that in **7b,** the Pauli repulsion is lower. In addition, the losses in electrostatic interaction with respect to **7b** are recovered by the corresponding orbital term. The dispersion contribution is also very similar, as indicated in the PEDA and the NCI plot (Figure 6). According to the NCI plot, the predominant contacts of the iodine atoms are with sulfur atoms, the methyl group, and the five-membered ring. The interaction with the five-membered ring stands out the most. In **7a**, it appears to be with the entire ring, while in **7b**, it is primarily with the nitrogen atom.

In the case of the pyridinium polymorph **8a**, DFT predicts a lattice energy 11.5 kcal/mol lower than **8b**. However, the corresponding PEDA suggests stronger interaction between the iodide and ammonium fragments in the latter, which can be explained in part by a decrease in the Pauli repulsion as well as a stronger orbital interaction between the fragments (Table 4). More specifically, the PEDA values indicate that both orbital and electrostatic interactions in the asymmetric system (**8a**) are stronger. The analysis suggests that the interaction between triiodides and pyridine moieties in both systems is mainly orbitalic, accounting for 63.1 and 81.9% of the attractive interactions. Remarkably, the steric hindrance is identical in both systems, but the dispersive forces are significantly higher in **8b**; that is, they account for 24.7% of the total interaction, compared to the asymmetric arrangement, which makes up 7.4% of the attractions between the components. In that sense, NCIs in **8a** show that the contacts are more centralized, i.e., both chlorine atoms point toward the same side and toward the iodine atoms, while in **8b**, the weak interactions are more dispersed. Indeed, more contacts are visible between iodine atoms and hydrogens of the amino ring (Figure 6).

3.3. Thermal Analysis

The thermal stability of the triiodide salts was studied by DSC/TGA and is summarized in Table 5. Plots of the DSC/TGA data and derivative mass loss are provided in the Supplementary Materials, Figures S13–S20. Data for polymorphs **1b**, **7b**, and **8a** are not included since those materials could not be isolated in sufficient quantity and purity for a reliable thermal analysis. In all cases, a melting endotherm is observed well prior to any mass loss. In triiodides **1**–**6**, decomposition appears in multiple consecutive steps based on the derivative mass loss. In general, the first of these decomposition steps correlates well to the loss of I_2 from the triiodide anion (typically within about 5% of that expected for I_2 loss). The loss of I_2 from the I_3^- anion is the typical pathway reported for triiodide decomposition in other triiodide salts, such as tetramethylammonium triiodide [57]. Decomposition of **7a** and **8b** may proceed in the same manner, though distinct steps in the derivative mass loss could not be reliably identified, giving the appearance of a single decomposition step. Regarding the melting points, for the tetraalkylammonium triiodide salts **1a** and **2**, we observe a decreasing melting point with increasing alkyl chain length, a trend generally

consistent with other tetraalkylammonium triiodides. For example, commercially available tetrabutylammonium triiodide is reported to melt at 69–71 °C, tetrapropylammonium triiodide around 98 °C [36], tetraethylammonium triiodide estimated around 115 °C [58], and tetramethylammonium triiodide also estimated around 115 °C [57]. A similar trend is observed in the melting points of the trialkylbenzylammonium triiodides **4**–**6** in the present study, where increasing alkyl chain length is correlated with lower melting points (as well as lower decomposition onsets). Trimethylphenylammonium triiodide, **3**, having the highest melting point observed in the current study, benefits from the short methyl groups as well as the stabilizing C-H···π contact involving the phenyl rings of neighboring molecules as described above.

Table 5. Thermal analysis of triiodides **1**–**8**. Values for the mass loss from the first decomposition step could not be determined (N.D.) for **7a** and **8b** since decomposition occurred in a single event with no apparent steps detected in the derivative mass loss.

Compound	Melting Point Onset (°C)	Decomposition Temperature Onset (°C)	Decomposition First Step Mass Loss (%)	Expected Mass Loss of I_2 (%)
1a	54.5	219.3	33.6	37.4
2	28.8	212.1	36.4	34.5
3	115.5	158.6	45.7	49.1
4	95.3	205.7	40.5	47.8
5	91.2	198.1	34.5	44.3
6	63.3	179.8	33.3	38.6
7a	90.7	212.9	N.D.	47.8
8b	61.5	176.7	N.D.	49.8

3.4. Triiodide Raman Spectroscopy

Symmetric and asymmetric Raman stretching bands of triiodides **1**–**8** were studied and summarized in Table 6 and shown in the Supplementary Materials, Figures S21–S28. The Raman stretching frequency of I-I in solid state I_2 occurs around 180 cm^{-1} [59] and moves to lower frequencies in systems where the I-I bond lengths of I_2 are lengthened through strong intermolecular interactions [60]. In the linear and symmetric triiodide anion, the symmetric stretching vibration is Raman active and typically produces a band at 100–120 cm^{-1} [1], while asymmetric stretching and bending vibrations are not Raman active. The asymmetric stretching vibration of a triiodide becomes Raman active when a distortion occurs in the triiodide anion. This leads to an additional band of medium intensity around 120–140 cm^{-1} [1,61]. The symmetric stretching bands are all well represented as strong bands in all the triiodides **1**–**8** studied here. For those salts containing asymmetric triiodide anions, the asymmetric stretching band is likewise observed. The asymmetric stretch for **3** appeared as a slight shoulder on the symmetric stretch and had to be approximated.

Table 6. Raman analysis of triiodides **1**–**8**.

Compound	I-I Symmetric Stretching (cm^{-1})	I-I Asymmetric Stretching (cm^{-1})
1a	112	135
2	113	-
3	113	118
4	112	125
5	111	119
6	112	138
7a	115	127
8b	114	-

4. Conclusions

Eight new triiodide salts are reported with full crystallographic characterization. Three of these salts exhibit polymorphic behavior, and the crystal structures of two polymorphs each of tetrapentylammonium triiodide, 3-methylbenzothiazolium triiodide, and 2-chloro-1-methylpyridinium triiodide, were compared. Each member of the polymorphic pairs exhibited significantly different packing patterns than its partner compound. Of particular note is that each pair of polymorphs was represented by one polymorph with an asymmetric triiodide anion and the other polymorph with a symmetric triiodide anion. A computational analysis of the polymorphs revealed more subtle differences in their isosurface plots. The most notable differences are observed in the interaction energy of polymorphs **1** and in the dispersive forces of polymorphs **8**. Both disparities can be explained by cation disordering. The ordered arrangement favors higher interaction energy in the former, while it favors weak interactions in the latter. The polymorphs were generally within an energetic threshold of one another, where both could be stable under the solution synthesis conditions employed. Mechanochemical synthesis was useful for obtaining the majority representation of one of the polymorphs in each case, but only in the case of 2-chloro-1-methylpyridinium triiodide did it lead to a single polymorphic phase. All eight triiodide salts that could be obtained in sufficient quantity and purity were studied by thermal analysis and Raman spectroscopy techniques. This, along with the structural characterization, establishes important baseline values for these compounds and bodes well for their future use in crystal engineering or in the preparation of new deep eutectic solvents.

Supplementary Materials: The following supporting information can be downloaded at https://www.mdpi.com/article/10.3390/cryst14121020/s1, Figures S1–S5: PXRD patterns; Figures S6–S12: additional packing diagrams and intermolecular interactions; Figures S13–S20: DSC/TGA; Figures S21–S28: Raman spectra.

Author Contributions: Conceptualization, T.W.H., C.D.M. and W.T.P.; methodology, M.B., K.K., C.V., R.S., J.B. and C.D.M.; validation, J.B. and C.D.M.; formal analysis, M.B., K.K., C.V., T.W.H., J.B., C.D.M. and W.T.P.; investigation, M.B., K.K., S.R.W., L.G., C.H., C.V., J.B. and C.D.M.; writing—original draft preparation, M.B., J.B., C.D.M. and W.T.P.; writing—review and editing, R.S., T.W.H., J.B., C.D.M. and W.T.P.; visualization, M.B., J.B. and C.D.M.; funding acquisition, C.D.M. and W.T.P. All authors have read and agreed to the published version of the manuscript.

Funding: This research was supported by the NASA SC Space Grant Consortium—award 80NSSC20M0153 and the Clemson University Summer CI + UR program.

Data Availability Statement: CCDC 2,376,730–2,376,740 contain the Supplementary Crystallographic Data for this paper. These data can be obtained from the CCDC, 12 Union Road, Cambridge CB2 1EZ, U.K.; Fax: +44-1223-336033.

Acknowledgments: The authors gratefully acknowledge computational resources utilized on the Palmetto Cluster. This material is based on work supported by the National Science Foundation under Grant Nos. MRI# 2024205, MRI# 1725573, and CRI# 2010270.

Conflicts of Interest: The authors declare no conflicts of interest. The funders had no role in the design of the study; in the collection, analyses, or interpretation of data; in the writing of the manuscript; or in the decision to publish the results.

References

1. Svensson, P.H.; Kloo, L. Synthesis, Structure, and Bonding in Polyiodide and Metal Iodide-Iodine Systems. *Chem. Rev.* **2003**, *103*, 1649–1684. [CrossRef] [PubMed]
2. Savastano, M. Words in supramolecular chemistry: The ineffable advances of polyiodide chemistry. *Dalton Trans.* **2021**, *50*, 1142–1165. [CrossRef] [PubMed]
3. Küpper, F.C.; Feiters, M.C.; Olofsson, B.; Kaiho, T.; Yanagida, S.; Zimmerman, M.B.; Carpenter, L.J.; Luther, G.W., III; Lu, Z.; Jonsson, M.; et al. Commemorating Two Centuries of Iodine Research: An Interdisciplinary Overview of Current Resarch. *Angew. Chem. Int. Ed.* **2011**, *50*, 11598–11620. [CrossRef] [PubMed]
4. Kloo, L.; Rosdahl, J.; Svensson, P.H. On the Intra- and Intermomlecular Bonding in Polyiodides. *Eur. J. Inorg. Chem.* **2002**, *2002*, 1203–1209. [CrossRef]

5. Savastano, M.; Bazzicalupi, C.; Bianchi, A. Novel cyclen-polyiodide complexes: A reappraisal of I-I covalent and secondary bond limits. *Dalton Trans.* **2022**, *51*, 10728–10739. [CrossRef]
6. Davy, H. Some Experiments and Observations on a new Substance which becomes a violet coloured Gas by Heat. *Philos. Trans. R. Soc. Lond.* **1814**, *104*, 74–93. [CrossRef]
7. Gay-Lussac, J.L. Mémoire sur l'iode. *Ann. Chim.* **1814**, *91*, 1–160.
8. Jones, G. On the Existence and Behavior of Complex Polyiodides. *J. Phys. Chem.* **1930**, *34*, 673–691. [CrossRef]
9. Jörgensen, S.M. Uber einige anorganische Superjodide. *J. Prakt. Chem.* **1870**, *2*, 347–360. [CrossRef]
10. He, S.; Wang, B.; Chen, H.; Tang, C.; Feng, Y. Preparation and antimicrobial properties of gemini surfactant supported triiodide complex system. *ACS Appl. Mater. Interfaces* **2012**, *4*, 2116–2123. [CrossRef]
11. Kaiho, T. Industrial applications of organic polyiodides. *Arkivoc* **2021**, *vii*, 66–78. [CrossRef]
12. Syrrokostas, G.; Tsamoglou, S.; Leftheriotis, G. Limitations imposed using an iodide/triiodide redox couple in solar-powered electrochromic devices. *Energies* **2023**, *16*, 7084. [CrossRef]
13. Gibson, E.; Le Pleux, L.; Fortage, J.; Pellegrin, Y.; Blart, E.; Odobel, F.; Hagfeldt, A.; Boschloo, G. Role of the triiodide/iodide redox couple in dye regeneration in p-type dye-sensitized solar cells. *Langmuir* **2012**, *28*, 6485–6493. [CrossRef] [PubMed]
14. Ma, J.Z.; Liu, M.; He, Y.; Zhang, J. Iodine redox chemistry in rechargeable batteries. *Angew. Chem. Int. Ed.* **2021**, *60*, 12636–12647. [CrossRef]
15. Li, P.; Li, C.; Guo, X.; Li, X.; Zhi, C. Metal-iodine and metal-bromine batteries: A review. *Bull. Chem. Soc. Jpn.* **2021**, *94*, 2036–2042. [CrossRef]
16. Gross, M.M.; Manthiram, A. Long-life polysulfide-polyhalide batteries with a mediator-ion solid electrolyte. *ACS Appl. Energy Mater.* **2019**, *2*, 3445–3451. [CrossRef]
17. Wlazlak, E.; Kalinowska-Tluscik, J.; Nitex, W.; Kljena, S.; Mech, K.; Macyk, W.; Szacilowski, K. Triiodide organic salts: Photoelectrochemistry at the border between insulators and semiconductors. *ChemElectroChem* **2018**, *5*, 3486–3497. [CrossRef]
18. Kahr, B.; Freudenthal, J.; Phillips, S.; Kaminsky, W. Herapathite. *Science* **2009**, *324*, 1407. [CrossRef]
19. Ajvazi, N.; Stavber, S. Electrophilic iodination of organic compounds using elemental iodine or iodides: Recent advances 2008–2021: Part I. *Compounds* **2022**, *2*, 3–24. [CrossRef]
20. Breugst, M.; von der Heiden, D. Mechanisms in iodine catalysis. *Chem. Eur. J.* **2018**, *24*, 9187–9199. [CrossRef]
21. Resnati, G.; Boldyreva, E.; Bombicz, P.; Kawano, M. Supramolecular interactions in the solid state. *IUCrJ* **2015**, *2*, 675–690. [CrossRef] [PubMed]
22. Peloquin, A.J.; McMillen, C.D.; Iacono, S.T.; Pennington, W.T. Crystal engineering using polyiodide halogen and chalcogen bonding to isolate the phenothiazinium radical cation and its rare dimer, 10-(3-Phenothiazinylidene)Phenothiazinium. *Chem. Eur. J.* **2021**, *27*, 8398–8405. [CrossRef] [PubMed]
23. Peloquin, A.J.; Kobra, K.; Li, Y.; McMillen, C.D.; Pennington, W.T. Halogen bonding of organoiodines and triiodide anions in $(NMe_3Ph)^+$ salts. *ChemPlusChem* **2021**, *86*, 612–621. [CrossRef] [PubMed]
24. Kobra, K.; O'Donnell, S.; Ferrari, A.; McMillen, C.D.; Pennington, W.T. Halogen bonding and triiodide asymmetry in cocrystals of triphenylmethylphosphonium triiodide with organoiodines. *New J.Chem.* **2018**, *42*, 10518–10528. [CrossRef]
25. Bartashevich, E.V.; Yushina, I.D.; Stash, A.I.; Tsirelson, V.G. Halogen Bonding and Other Iodine Interactions in Crystals of Dihydrothiazolo(oxazino)quinolinium Oligoiodides from the Electron-Density Viewpoint. *Cryst. Growth Des.* **2014**, *14*, 5674–5684. [CrossRef]
26. Savastano, M.; Bazzicalupi, C.; Garcia, C.; Gellini, C.; de la Torre, M.D.L.; Mariani, P.; Pichierri, F.; Bianchi, A.; Melguizo, M. Iodide and triiodide anion complexes involving anion-π interactions with a tetrazine-based receptor. *Dalton Trans.* **2017**, *46*, 4518–4529. [CrossRef]
27. Ayres, L.B.; Bandara, M.; McMillen, C.D.; Pennington, W.T.; Garcia, C.D. eutXG: A gradient boosting model to predict the melting point of deep eutectic solvents. *ACS Sustain. Chem. Eng.* **2024**, *12*, 11260–11273. [CrossRef]
28. Talip, R.A.A.; Yahya, W.Z.N.; Bustam, M.A. Understanding the physicochemical and transport properties of pyrazolium based ionic liquids bering iodide and triiodide anions. *J. Mol. Liq.* **2022**, *346*, 118270. [CrossRef]
29. Koyakkat, M.; Moriyama, K.; Asakura, S.; Kawamoto, H. Deep eutectic solvents based on ammonium iodide and iodine possessing high elelctrical conductivity. *J. Mol. Liq.* **2023**, *384*, 122250. [CrossRef]
30. Shi, R.; Yu, D.; Zhou, F.; Yu, J.; Mu, T. An emerging deep eutectic solvent based on halogen-bonds. *Chem. Commun.* **2022**, *58*, 4607–4610. [CrossRef]
31. Abranches, D.O.; Coutinho, J.A.P. Everything You Wanted to Know about Deep Eutectic Solvents but Were Afraid to Be Told. *Ann. Rev. Chem. Biomol. Engin.* **2023**, *14*, 141–163. [CrossRef]
32. Martins, M.A.R.; Pinho, S.P.; Coutinho, J.A.P. Insights into the nature of eutectic and deep eutectic mixtures. *J. Solut. Chem.* **2019**, *48*, 7962–7982. [CrossRef]
33. Bakshi, P.K.; James, M.A.; Cameron, T.S.; Knop, O. Polyhalide anions in crystals. Part 1. Triiodides of the Me_4N^+, Me_4P^+, quinuclidinium, 1-azoniapropellane, and 1,4-diazoniabicyclo[2.2.2]octane ($DabcoH_2^{2+}$) cations, and 1,10-phenanthrolinium(1+) tribromide. *Can. J. Chem.* **1996**, *74*, 559–573. [CrossRef]
34. Ishigami, H.; Sumita, M.; Tsunashima, Y.; Hori, T.; Sato, S.; Shiro, M. Phase Transition in $C_4H_{12}NI{\cdot}I_2$. *J. Kor. Phys. Soc.* **2003**, *42*, 1237–1239.

35. Migchelsen, T.; Vos, A. The crystal structure of two modifications of tetraethylammonium triiodide, $(C_2H_5)_4NI_3$. *Acta Cryst.* **1967**, *23*, 296–804. [CrossRef]
36. Tebbe, K.-F.; Gilles, T. Über Tetra(n-propyl)ammoniumpolyiodide (n-$Pr_4N)I_n$ mit n = 3, 5, 7: Darstellung und strukturelle Charakterisierung eines Triiodids (n-$Pr_4N)I_3$, eines Pentaiodids (n-$Pr_4N)I_5$ und eines Heptaiodids (n-$Pr_4N)I_7$. *Z. Anorg. Allg. Chem.* **1996**, *622*, 1587–1593. [CrossRef]
37. Herbstein, F.H.; Kaftory, M.; Kapon, M.; Saenger, W. Structures of three crystals containing approximately-linear chains of triiodide anions. *Z. Krist. Cryst. Mater.* **1981**, *154*, 11–30.
38. El Essawi, M.; El Khalik, S.A.; Berthold, H.J.; Wartchow, R. Synthese und Kristallstruktur von Triphenylmethylphosphoniumtriiodid $[P(C_6H_5)_3CH_3]I_3$. *Z. Naturforsch.* **1991**, *46b*, 703–708. [CrossRef]
39. Chow, H.; Dean, P.A.W.; Craig, D.C.; Lucas, N.T.; Scudder, M.L.; Dance, I.G. The subtle tetramorphism of $MePh_3P^+I_3^-$. *New J. Chem.* **2003**, *27*, 704–713. [CrossRef]
40. Kobra, K.; Li, Y.; Sachdeva, R.; McMillen, C.D.; Pennington, W.T. New polymorphism and structrual sensitivity in triphenylmethylphosphonium trihalide salts. *New J. Chem.* **2019**, *43*, 12702–12710. [CrossRef]
41. *Apex3*; Bruker AXS Inc.: Madison, WI, USA, 2015.
42. Sheldrick, G.M. *SHELXT*–Integrated space-group and crystal -structure determination. *Acta Crystallogr. Sect. A Found. Adv.* **2015**, *71*, 3–8. [CrossRef] [PubMed]
43. Sheldrick, G.M. Crystal structure refinement with *SHELXL*. *Acta Crystallogr. Sect. C Struct. Chem.* **2015**, *71*, 3–8. [CrossRef]
44. Perdew, J.P.; Ruzsinszky, A.; Csonka, G.I.; Vydrov, O.A.; Scuseria, G.E.; Constantin, L.A.; Zhou, X.L.; Burke, K. Restoring the density-gradient expansion for exchange in solids and surfaces. *Phys. Rev. Lett.* **2008**, *100*, 136406. [CrossRef] [PubMed]
45. Giannozzi, P.; Baroni, S.; Bonini, N.; Calandra, M.; Car, R.; Cavazzoni, C.; Ceresoli, D.; Chiarotti, G.L.; Cococcioni, M.; Dabo, I.; et al. QUANTUM ESPRESSO: A modular and open-source software project for quantum simulations of materials. *J. Phys. Condens. Matter* **2009**, *21*, 395502. [CrossRef] [PubMed]
46. Giannozzi, P.; Andreussi, O.; Brumme, T.; Bunau, O.; Nardelli, M.B.; Calandra, M.; Car, R.; Cavazzoni, C.; Ceresoli, D.; Cococcioni, M.; et al. Advanced capabilities for materials modelling with QUANTUM ESPRESSO. *J. Phys. Condens. Matter* **2017**, *29*, 465901. [CrossRef]
47. Prandini, G.; Marrazzo, A.; Castelli, I.E.; Mounet, N.; Marzari, N. Precision and efficiency in solid-state pseudopotential calculations. *Npj Comput. Mater.* **2018**, *4*, 72. [CrossRef]
48. Grimme, S. Semiempirical GGA-type density functional constructed with a long-range dispersion correction. *J. Comput. Chem.* **2006**, *27*, 1787–1799. [CrossRef]
49. Raupach, M.; Tonner, R. A periodic energy decomposition analysis method for the investigation of chemical bonding in extended systems. *J. Chem. Phys.* **2015**, *142*, 194105. [CrossRef]
50. Sun, J.; Ruzsinszky, A.; Perdew, J.P. Strongly Constrained and Appropriately Normed Semilocal Density Functional. *Phys. Rev. Lett.* **2015**, *115*, 036402. [CrossRef]
51. Grimme, S.; Ehrlich, S.; Goerigk, L. Effect of the Damping Function in Dispersion Corrected Density Functional Theory. *J. Comput. Chem.* **2011**, *32*, 1456–1465. [CrossRef]
52. Brandenburg, J.G.; Bates, J.E.; Sun, J.; Perdew, J.P. Benchmark tests of a strongly constrained semilocal functional with a long-range dispersion correction. *Phys. Rev. B* **2016**, *94*, 115144. [CrossRef]
53. Van Lenthe, E.; Baerends, E.J. Optimized slater-type basis sets for the elements 1-118. *J. Comput. Chem.* **2003**, *24*, 1142–1156. [CrossRef] [PubMed]
54. Contreras-García, J.; Boto, R.A.; Izquierdo-Ruiz, F.; Reva, I.; Woller, T.; Alonso, M. A benchmark for the non-covalent interaction (NCI) index or... is it really all in the geometry? *Theor. Chem. Acc.* **2016**, *135*, 242. [CrossRef]
55. Lefebvre, C.; Rubez, G.; Khartabil, H.; Boisson, J.C.; Contreras-García, J.; Hénon, E. Accurately extracting the signature of intermolecular interactions present in the NCI plot of the reduced density gradient versus electron density. *Phys. Chem. Chem. Phys.* **2017**, *19*, 17928–17936. [CrossRef] [PubMed]
56. Lefebvre, C.; Klein, J.; Khartabil, H.; Boisson, J.C.; Henon, E. IGMPlot: A program to identify, characterize, and quantify molecular interactions. *J. Comput. Chem.* **2023**, *44*, 1750–1766. [CrossRef]
57. Yushina, I.; Rudakov, B.; Krivtsov, I.; Bartashevich, E. Thermal decomposition of tetraalkylammonium iodides. *J. Therm. Anal. Calorim.* **2014**, *118*, 425–429. [CrossRef]
58. Wang, Y.; Xue, Y.; Wang, X.; Cui, Z.; Wang, L. The stable polyiodides: Experimental and theoretical studies of formation mechanism. *J. Mol. Struct.* **2014**, *1074*, 231–239. [CrossRef]
59. Anderson, A.; Sun, T.S. Raman spectra of molecular crystals I. Chlorine, bromine, and iodine. *Chem. Phys. Lett.* **1970**, *6*, 611–616. [CrossRef]
60. Deplano, P.; Devillanova, F.A.; Ferrraro, J.R.; Isaia, F.; Lippolis, V.; Mercuri, M.L. On the Use of Raman Spectroscopy in the Characterization of Iodine in Charge-Transfer Complexes. *Appl. Spectrosc.* **1992**, *46*, 1625–1629. [CrossRef]
61. Yushina, I.D.; Kolesov, B.A.; Bartashevich, E.V. Raman spectroscopy study of new thia- and oxazinoquinolinium triiodides. *New J. Chem.* **2015**, *39*, 6163–6170. [CrossRef]